

The Influence of Surface Ligands on Energetics at FASnI₃/C₆₀ Interfaces and Their Impact on Photovoltaic Performance

Alex M. Boehm,[†] Tuo Liu,[†] So Min Park,^{‡,†} Ashkan Abtahi,^{§,†} Kenneth R. Graham^{†,}*

[†]Department of Chemistry, [‡]Department of Chemical and Materials Engineering, and [§]Department of Physics and Astronomy, University of Kentucky, Lexington, Kentucky 40506, United States

ABSTRACT

Interfacial chemistry and energetics significantly impact the performance of photovoltaic devices. In the case of Pb-containing organic metal halide perovskites, photoelectron spectroscopy has been used to determine the energetic alignment of frontier electronic energy levels at various interfaces present in the photovoltaic device. For the Sn-containing analogues, which are less toxic, no such measurements have been made. Through a combination of ultraviolet, inverse, and X-ray photoelectron spectroscopy (UPS, IPES, and XPS, respectively) measurements taken at varying thickness increments during stepwise deposition of C₆₀ on FASnI₃, we present the first direct measurements of the frontier electronic energy levels across the FASnI₃/C₆₀ interface. The results show band bending in both materials and transport gap widening in FASnI₃ at the interface with

C₆₀. The XPS results show that iodide diffuses into C₆₀ and results in *n*-doping of C₆₀. This iodide diffusion out of FASnI₃ impacts the valence and conduction band energies of FASnI₃ more than the core levels, with the core level shifts displaying a different trend than the valence and conduction band. Surface treatment of FASnI₃ with carboxylic acids and bulky ammonium substituted surface ligands results in slight alterations in the interfacial energetics, and all surface ligands result in similar or improved PV performance relative to the un-treated devices. The greatest PV stability results from treatment with a fluorinated carboxylic acid derivative; however, iodide diffusion is still observed to occur with this surface ligand.

KEYWORDS: formamidinium tin iodide, perovskite solar cell, photoelectron spectroscopy, inverse photoelectron spectroscopy, interfacial energetics, surface modification, ion diffusion

INTRODUCTION

Interfaces play a massive role in determining the performance of photovoltaic (PV) devices, including those based on organic metal halide perovskites (HPs).¹⁻⁷ Halide perovskite solar cells (PSCs) typically rely on a *p-i-n* (inverted) or *n-i-p* (normal) device architecture, whereby the HP is the *i* layer and carries out the majority of photon absorption and the *n* and *p* layers are the electron transporting layer (ETL) and hole transporting layer (HTL), respectively. In an operating PSC electrons and holes must be transferred across the HP/ETL and HP/HTL interfaces, respectively, to reach the electrodes. In an ideal case, charge transfer across these interfaces occurs with minimal recombination. However, in reality these interfaces are plagued by severely increased recombination as compared to the bulk of the HP.^{2,4,8-10} Furthermore, ion transfer across these interfaces is a major degradation pathway in the PV device,¹¹ as is water

ingression across these interfaces and into the HP layer. With this in mind, understanding and controlling these interfaces is a key aspect in improving the performance of PSCs.

Lead (Pb) containing HPs have been the subject of massive research interest, which has resulted in the power conversion efficiencies (PCEs) climbing from a few percent to nearly 25% over the past decade.^{12,13} Not surprisingly, surfaces and interfaces in Pb-based HPs have been an area of growing interest. Here, researchers have shown that surface recombination rates are commonly three-orders of magnitude faster than bulk recombination rates,^{2,4,8} and that interfacial recombination leads to major performance losses in PV devices.⁹ One factor that determines surface and interfacial recombination rates is the concentration of trap states that can serve as recombination centers. Passivation of these trap states thus provides one means to decrease recombination rates.^{2,8,14} Another factor that will influence interfacial recombination rates and interfacial charge transfer processes is the interfacial energy landscape.^{1,10,15–18} Non-ideal interfacial energetics can result in charge build up at the interfaces, which will result in increased interfacial recombination rates. As such, measurements of energetics at interfaces with Pb-based HPs are prevalent in the literature.^{15,19–25} These interfacial energetic measurements provide important data for understanding the physical processes occurring within the device and highlight that optimization of interfacial energetics may lead to further increased PV performance.^{10,17,18}

Energy level alignments at Pb-based HP/HTL and HP/ETL interfaces and their influence on charge extraction, charge carrier recombination, and PV performance are not well established and are a subject of active research.^{1,10,15} Commonly, with organic transport layers a flat band condition is maintained within the HP;^{21,26,27} however, interfacial dipoles and band bending in

the HTL or ETL are occasionally observed.^{24,28-30} In part, the lack of clear agreement on these interfacial energetics may arise from differences in surface stoichiometry,¹⁶ surface defect states,³⁰ underlying substrates and initial work function,^{16,31} the difficulty in assigning VBM and CBM values due to the low density of states at the band edge,^{32,33} surface photovoltage effects,³⁴ or degradation processes occurring during measurement.^{35,36} Unfavorable interfacial energetics, for example where a barrier to charge extraction exists, have been observed to decrease PV performance.¹⁷ Similarly, charge transport layers that are not selective, i.e., a barrier to extraction of the opposite carrier does not exist, have also been observed to result in lower PV performance.^{10,37} In general, although some conflicting reports do exist,³⁸ so long as a barrier to charge extraction is not present and the transport layer is selective, the performance of Pb-based PSCs does not require that the IE or EA of the HTL or ETL be exactly matched to those of the HP.^{1,37} That said, even small losses due to less than optimal interfacial energetics should be reduced to maximize the PV performance.

Surface ligands provide a means to passivate surface defect states,^{14,39-42} decrease diffusion of species across an interface,³⁹ and manipulate interfacial energetics.⁴³ Application of surface ligands to Pb-based HP thin films has resulted in increased PL intensity,^{14,40} reduced recombination rates, improved stability,^{39,44} and improved PV performance.^{39,40,44} Although numerous reports show that surface ligand treatment of HPs can improve PV performance, it is not yet clear how these ligands influence the interfacial energy landscape. Here, UPS, IPES, and XPS measurements recorded at varying thickness increments are necessary to determine the complete energy landscape, yet these measurement series on surface ligand treated interfaces are not yet apparent in the literature. Moving forward, it will be important to clearly identify how

surface ligands impact interfacial energetics and how these energetics alter interfacial charge transfer processes and PV performance.

As discussed, most work on PSCs has focused on Pb-based HPs; however, Pb renders these materials and devices toxic. Although they have significantly lower PCEs,^{45,46} tin (Sn) containing HPs present a promising alternative to their Pb containing counterparts due to their lower toxicity. Surface states and interfaces in these Sn-containing HPs are significantly less explored and it is likely that these surfaces and interfaces are hugely important for improving Sn-based HP materials and PV device performance and stability. In this article, we present the first measurements of energetics at interfaces between FASnI₃ (FA=formamidinium) and C₆₀, where FASnI₃ represents the most commonly used Sn-based HP in PVs and C₆₀ is one of the most commonly used ETL materials. The interfacial energetics show a favorable energy landscape for electron transfer to occur from FASnI₃ to C₆₀ and an unfavorable energy landscape for hole transfer. The XPS measurements also show clear evidence of I⁻ diffusion into the C₆₀ layer and this I⁻ diffusion is related to the observed interfacial energetics. Furthermore, we show how surface ligand treatment impacts the interfacial energy landscape and PV performance and stability of inverted devices with C₆₀ as the ETL.

EXPERIMENTAL SECTION

Materials.

Perovskite precursors and solvents include Tin (II) Iodide (SnI₂, 99.999%), anhydrous N,N-Dimethylformamide (DMF, 99.8%), and anhydrous toluene (99.8%) all purchased from Alfa Aesar. Formamidinium Iodide (FAI, Greatcell Solar), Tin (II) Fluoride (SnF₂, 99%) and

anhydrous anisole (99%) were purchased from Acros Organics. Dimethyl sulfoxide (DMSO, 99.9%, Seccosolv) was purchased from Millipore Sigma. All listed solvents were degassed using at least three freeze-pump-thaw cycles. Contacts and transporting layers consisted of indium tin oxide (ITO) coated glass substrates from Tinwell Tech. ($15 \Omega/\square$), PEDOT:PSS (Clevios P VP AI 4083), C₆₀ (Nano-C, 99.5%), bathocuproine (BCP, TCI, >99%) and silver (Ag, Kurt J. Lesker, 99.999%). C₆₀ used in the interfacial studies was thoroughly purified through a series of heating cycles under high vacuum. Surface ligands include octanoic acid (OCA, 98+%, Alfa Aesar), trimethylphenylammonium chloride (TMPA-Cl, >98%, TCI), and 2H,2H,3H,3H-Perfluorononanoic acid (FNCA, >96%, Sigma Aldrich).

UPS, XPS and IPES measurements.

Photoelectron spectroscopy measurements were conducted in a PHI 5600 UHV system (typical base pressure 3×10^{-10} mbar). Solution processed films were fabricated and transferred completely under a nitrogen atmosphere (typically <0.1 ppm H₂O and O₂) and thermally evaporated films were loaded without breaking vacuum such that no sample was exposed to air. All measurements were completed within 24 hours of sample fabrication to minimize sample degradation or surface contamination. UPS and XPS measurements both employed an 11-inch diameter hemispherical electron energy analyzer and multichannel detector. The excitation source for UPS was an Excitech H Lyman- α lamp (E-LUXTM121) with an excitation energy of 10.2 eV, which is detailed in our previous work.⁴⁷ All UPS measurements were recorded with -5V sample bias and a pass energy of 5 eV. XPS measurements used a dual anode Mg-Al x-ray excitation source (Al *ka* emission 1486.6 eV, and Mg *ka* at 1256.6 eV); and a pass energy of 30 eV.

IPES measurements were performed in the Bremsstrahlung isochromat mode with electron kinetic energies below 5 eV and an emission current of 2 μA to minimize sample damage. A Kimball Physics ELG-2 electron gun equipped with a low temperature (1150K) BaO cathode was used to generate the low energy electron beam. Emitted photons were collected with a bandpass photon detector consisting of an optical bandpass filter (254 nm, Semrock) and a photomultiplier tube (R585, Hamamatsu Photonics). During all IPES measurements the UHV chamber was blacked-out to exclude external light and samples were held under a -20 V bias.

Perovskite samples for photoelectron spectroscopy studies were prepared on PEDOT:PSS covered ITO substrates using the procedure described in the device fabrication section. During the incremental depositions pressure was maintained below 5×10^{-7} mbar in the deposition chamber and low deposition rates of $<0.5 \text{ \AA/s}$ were used and closely monitored with quartz crystal microbalances.

PV device fabrication and characterization.

Patterned 2x2 cm ITO-coated glass substrates were cleaned by sequential sonication in deionized water with sodium dodecyl sulfate, pure deionized water, acetone, and 2-propanol each for 15 minutes. After drying with compressed air the ITO-coated substrates were UV-ozone treated for 15 minutes. Immediately following UV-ozone treatment 175 μL of room temperature, 0.45 μm nylon filtered, PEDOT:PSS solution was spun cast at 4,000 rpm for 45 s with an acceleration of 800 rpm/s before annealing at 120 $^{\circ}\text{C}$ for 15 minutes in air. The samples were then transferred into a N_2 filled glove box (typically <0.1 ppm O_2 and H_2O) for all further processing.

Inside the glovebox a 1.1M FASnI₃ precursor solution with 10 mol% SnF₂ was prepared by dissolving SnI₂, FAI, and SnF₂ in a 1:1:0.1 molar ratio using a 70:30 (V:V) mixture of anhydrous and degassed DMF and DMSO. This solution was mixed at 750 rpm without heat for at least 2.5 hours before spin casting. Following a similar procedure from the literature,⁴⁸ the perovskite solution was then deposited by spin coating 75 μ L of solution at 9,999 rpm (with maximum acceleration) for 2 s before a 25 s ramp down to 0 rpm (400 rpm/s deceleration). The substrates were then immersed in anisole for approximately 4 seconds before being placed back on the spin coater and spun at 4,000 rpm for 30 s (2,000 rpm/s acceleration) to dry. When 5 s remained in this spin cycle 120 μ L of toluene was quickly dropped on the substrate surface from a height of approximately 1 cm as a second anti-solvent treatment. Samples then sat at room temperature for 5 minutes before annealing at 130 °C for 15 minutes. The films were then transferred to a thermal evaporator where 40 nm C₆₀ and 8 nm BCP were sequentially deposited at a pressure of approximately 1×10^{-6} mbar. Finally, 100 nm Ag electrodes were deposited through a shadow mask defining cells with an area of 0.1 cm². PV performance was measured inside the glove box using a solar simulator (ABET technologies, 11002) at 100 mW/cm² illumination (AM 1.5G). The solar intensity was adjusted using a calibrated photodiode from Thorlabs (FDS1010-CAL) with a KG3 filter.

Vapor treatment with surface ligands.

Treatment of the FASnI₃ films with surface ligands occurred after annealing was completed. The bottom half of a petri dish was placed on a hotplate set to the desired temperature (140 °C for TMAPA-Cl and 90 °C for FNCA and OCA) and given 2 minutes to warm up. During this time FASnI₃ samples were affixed to the lid of the petri dish using Kapton tape such that the

perovskite film was oriented down. After 2 minutes passed 5-10 mg (or 10-20 μL) of the desired ligand was placed in center of the warm petri dish bottom before immediately capping with the lid containing the affixed samples. The dishes and samples were left unperturbed for 2 minutes before removing from the hotplate and immediately retrieving the samples from the petri dish lid. As a check for the impact this additional heating may have, this procedure was performed without the inclusion of a surface ligand at temperatures up to 200 $^{\circ}\text{C}$; no changes in PV performance were observed. Additionally, in device sets where some samples are not treated with surface ligands, or multiple surface ligands are being used, great care is taken to minimize chances for contamination by placing samples in heat-sealed bags or moving them into an adjacent antechamber or glovebox.

UV-Vis absorbance and photoluminescence measurements.

UV-Vis absorbance and photoluminescence measurements are carried out inside a N_2 -filled glovebox with an Ocean Optics QE Pro high-performance spectrometer. UV-vis absorbance measurements are performed inside an integrating sphere whereas photoluminescence measurements are performed in an open fixed geometry setup to reduce re-absorption effects. FASnI_3 samples are prepared on glass substrates and modified with surface ligands using the procedures already described.

RESULTS AND DISCUSSION

Low energy ultraviolet photoelectron spectroscopy (UPS) and inverse photoelectron spectroscopy (IPES) are employed to probe the frontier occupied and unoccupied states respectively, at FASnI_3 surfaces and interfaces. Both our experimental systems rely on lower

energies than typically used, with our UPS system using 10.2 eV for excitation,⁴⁷ compared with the most commonly used He I excitation source at 21.22 eV, and our IPES system probing 4.88 eV photons and using electrons with kinetic energies of 0 to 5 eV,⁴⁹ as compared to the traditional laboratory based IPES system that probes 10 eV photons and uses electrons with kinetic energies of 5-15 eV. Both systems have been shown to significantly reduce sample damage in organic semiconductors and are expected to have a similar effect on reducing sample damage in HPs.^{47,49}

The FASnI₃ samples analyzed throughout this paper are of high quality, as evidenced by their reasonable PV performance of 3 to 5%.⁴⁵ In addition, XPS was routinely performed to ensure lack of extraneous surface contamination and appropriate surface stoichiometry. **Figure 1** shows the valence and conduction band regions of neat FASnI₃ measured with UPS and IPES on a semilogarithmic plot. Both spectra have been adjusted along the x-axis such that the vacuum level corresponds to E= 0 eV, meaning that the ionization energy (IE) and electron affinity (EA) can be determined directly from the onsets of the valence and conduction bands. These positions, marked with solid vertical blue lines, are determined with a Gaussian fit to the lowest binding energy feature for UPS and highest binding energy feature for IPES as described in the Supporting Information and SI **Figure S1**. This results in an IE of 5.31 eV and EA of 3.93 eV for the neat perovskite film. Reported literature values for FASnI₃ show significant variation in the IE, covering a range from 4.7-6 eV.⁵⁰⁻⁵³ These discrepancies in reported values stem from a variety of factors, such as differences in surface composition,¹⁶ film fabrication conditions,^{54,55} and onset determination methods for the low density of states at the band edges.^{32,33} Our value of 5.31 eV falls near the center of this range and matches well the recent work from the Olthof

group that utilized both experimental and computational studies to determine energy levels for a variety of perovskite compositions.³² Far fewer reports can be found for the electron affinity of FASnI₃ and our value of 3.93 eV does deviate slightly from the 4.12 eV value reported by the Olthof group.³² From these energetic values the transport gap for FASnI₃ is determined to be 1.38 eV. This corresponds well with the experimental optical gap of 1.35 eV from absorption measurements as shown in SI **Figure S2** and other reports of the optical gaps derived from absorption measurements and Tauc plots.⁵²

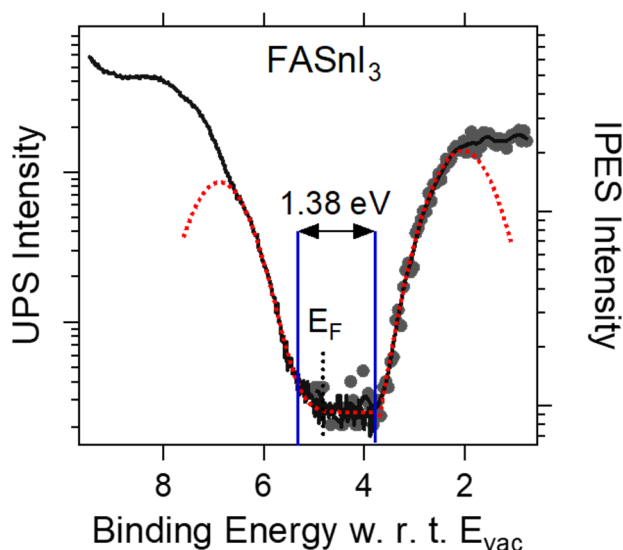
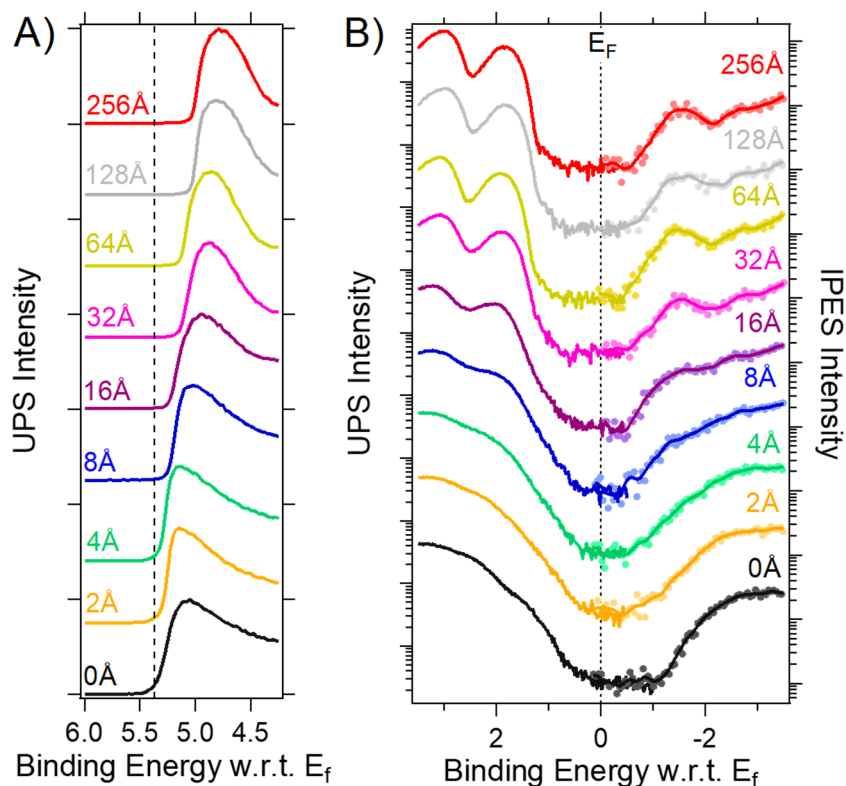


Figure 1. UPS and IPES spectra of a FASnI₃ film.

To investigate the energetic structure at the FASnI₃/C₆₀ interface we performed a series of incremental depositions of C₆₀ on a FASnI₃ film and carried out UPS, IPES, and XPS measurements after each deposition step. Here, C₆₀ is a common ETL material for Sn-based PSCs in the inverted structure and a close analog for solution processable fullerene derivatives. **Figure 2A and B** show the evolution of the UPS and IPES spectra on a semilogarithmic plot as

the thickness of C₆₀ is increased from 0 to 256 Å. Note that the x-axis is plotted relative to the Fermi energy (E_f). The position of the secondary electron cut-off (SECO) from UPS shows a consistent trend towards lower binding energies as the C₆₀ thickness increases, indicating an upwards shift in the vacuum level. In the onset region C₆₀ HOMO and LUMO features grow in quickly and the position of E_F within the gap moves towards the unoccupied states. The energy diagram shown in **Figure 2C** was constructed based upon analysis of the UPS, IPES, and XPS spectra, as discussed in the proceeding paragraphs.



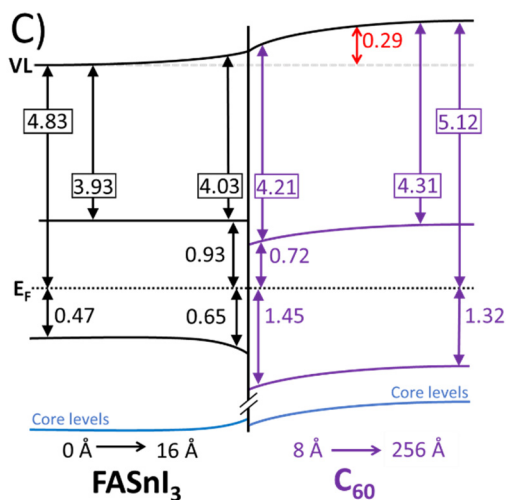


Figure 2. Secondary electron cutoff region (A) and onset region (B) recorded using UPS and IPES during the stepwise deposition of C₆₀ on FASnI₃ with no surface ligand treatment. Results are summarized in a schematic diagram of the energy levels (C). Work functions were determined from the SECO in UPS.

The XPS spectra taken at each thickness increment during the deposition of C₆₀ of FASnI₃ are displayed in **Figure 3**. Initial XPS measurements show a surface stoichiometry of 1:1.7: 1.1: 3 for C: N: Sn: I which is close to the ideal stoichiometry. Here, all XPS peaks shift slightly upon deposition of C₆₀, indicating the presence of some band bending occurring in the HP. Upon deposition of 2 Å C₆₀, all XPS peaks from FASnI₃ shift to higher binding energies by 0.22 to 0.29 eV. This shift in the core levels does not follow the change in the work function, which increases by only 0.04 eV upon deposition of 2 Å C₆₀. Following this initial peak shift to higher binding energies, the XPS peaks from FASnI₃ all gradually shift to lower energies by *ca.* 0.3 eV as up to 32 Å of C₆₀ is deposited, as shown in SI **Figure S3**. With each consecutive C₆₀ deposition the XPS peak intensities of Sn and I are attenuated while the non-FA C peak

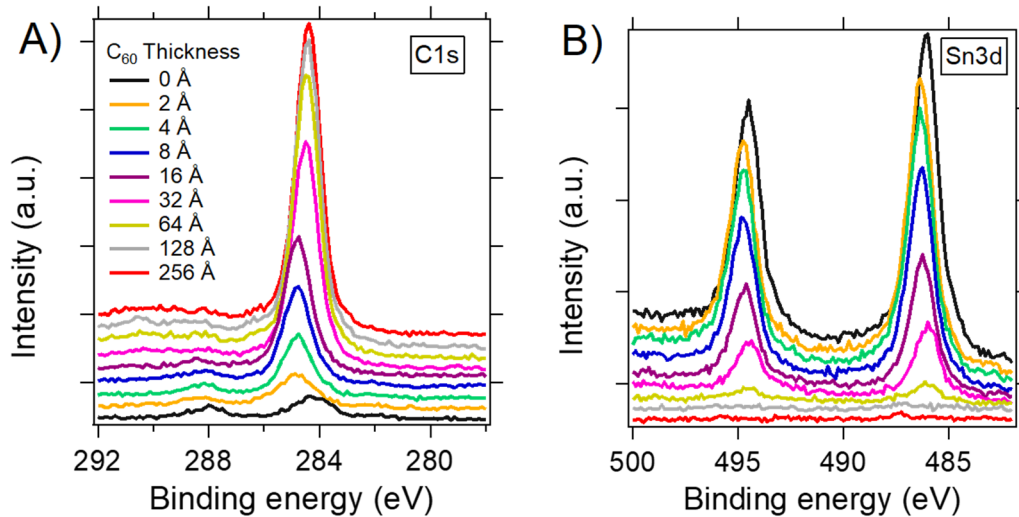
increases, as expected; however, I remains weakly visible even after 256 Å of C₆₀ is deposited. In contrast, Sn is completely absent from the XPS spectra when only 128 Å of C₆₀ is deposited, which is expected if a clean bilayer is formed. Additionally, no change in the ratio of Sn(II):Sn(IV) is observed throughout the stepwise series as shown in SI **Figure S4**. Considering that Sn is absent, yet I is clearly apparent at both 128 and 256 Å of C₆₀, we conclude that I must be diffusing into the C₆₀ layer. Notably, this I⁻ diffusion is not evident in stepwise deposition measurements of C₆₀ on MAPbI₃.⁵⁶

The XPS data in **Figure 3C** shows that the I 3d_{5/2} peak appears at between 618.84 and 619.08 eV at thicknesses between 0 and 32 Å of C₆₀ and increases by approximately 1 eV to 619.85 eV at a thickness of 256 Å. **Figure 3D** shows a closer look at the I 3d_{5/2} region at higher C₆₀ thickness. At a C₆₀ thickness of 32 Å, the I 3d_{5/2} region can be adequately fit with a single peak at 618.75 eV. However, at a C₆₀ thickness of 64 Å a broadening towards higher BE is apparent and the data is better fit with two peaks, one at 618.73 and another at 619.9 eV. The same is observed with 128 Å where the higher BE I peak is now dominant. Finally, at 256 Å of C₆₀ only the higher BE I species is visible at 619.85 eV. The shifts in the I 3d_{5/2} peak position are consistent with I⁻ converting to I₂ or I₃⁻, with both I₂ or I₃⁻ appearing at higher binding energies due to the change in the average oxidation state of I. The change in I⁻ to I₂ or I₃⁻ strongly suggests that I⁻ is reducing C₆₀ and resulting in *n*-doped C₆₀⁻. This mechanism is supported by previous literature where halide ions have been used to *n*-dope fullerenes through the introduction of ammonium halide salts, with the *n*-doping resulting in large increases in the electrical conductivity.⁵⁷⁻⁶²

To quantify the amount of iodide diffusing into the C_{60} layer and the resulting iodide deficiency at the $FASnI_3$ surface, the XPS peak ratio between the C1s of C_{60} and the I 3d_{5/2} of the higher BE I species (>619.5 eV) was examined and the extent of iodide deficiency estimated. As detailed in the Supporting Information, the ratio of C:I can be determined at C_{60} thicknesses of 64 Å and greater and is fairly consistent at 330:1 or 5-6 C_{60} molecules per I atom. Using simple volume calculations, we can relate the amount of I in the C_{60} overlayer to the depletion of the $FASnI_3$ surface. A plot showing the percent iodide deficiency vs. the thickness of the iodide depletion layer as a function of the C_{60} overlayer thickness is shown in SI **Figure S5**. We estimate that at lower C_{60} thicknesses (<32 Å) the iodide deficiency of the $FASnI_3$ surface will be 5-20%, while at larger C_{60} thickness of 256 Å or 400 Å (where 400 Å is the thickness used in devices) the level of iodide deficiency could be greater than 75% for the first few layers (~5 nm). If the iodide deficiency is uniform across the entire thickness of the film there will be a 3% iodide deficiency when 400 Å of C_{60} is deposited. These levels of iodide deficiency, especially in the case of greater iodide deficiency near the C_{60} interface, could have major impacts on the crystalline structure and energetics in the near-surface region of $FASnI_3$.

The energy diagram in **Figure 2C** was constructed from a combination of the UPS, IPES, and XPS data and shows the evolution of the $FASnI_3$ and C_{60} energetics from 0-16 Å and 8-256 Å respectively. The UPS and IPES data were fit using a linear combination of the pure $FASnI_3$ spectra and the C_{60} spectra at 256 Å thickness to extract the electronic energy levels from both materials, as evident in SI **Figure S6**. While gaussian fits on a logarithmic scale are used to determine the band edges for $FASnI_3$, values for C_{60} are extracted using linear extrapolation on a linear scale. The energy diagram shows that when 8 Å C_{60} is deposited, the LUMO of C_{60} lies

0.18 eV lower in energy than the conduction band minimum (CBM) of FASnI₃, which is a favorable energy landscape for transferring electrons from FASnI₃ to C₆₀. Furthermore, the HOMO of C₆₀ lies 0.80 eV lower in energy than the valence band maximum (VBM) of FASnI₃, thereby providing a barrier to hole transfer from FASnI₃ to C₆₀. Both the HOMO and LUMO bands of C₆₀ display similar upward band bending as the thickness increases. This upward band bending of C₆₀ away from the interface is similar to that observed for C₆₀ on MAPbI₃.^{56,63} Although the EA of C₆₀ increases with thickness, the LUMO of C₆₀ bends upwards because of the more rapidly changing work function. The band bending observed in the C₆₀ HOMO is consistent with the C 1s shift observed in the XPS data; likewise, the bending of the LUMO is consistent with increased *n*-doping of C₆₀ near the FASnI₃ interface. That is, the C₆₀ LUMO is closer to E_F near the interface and gradually moves farther away as the C₆₀ thickness increases.



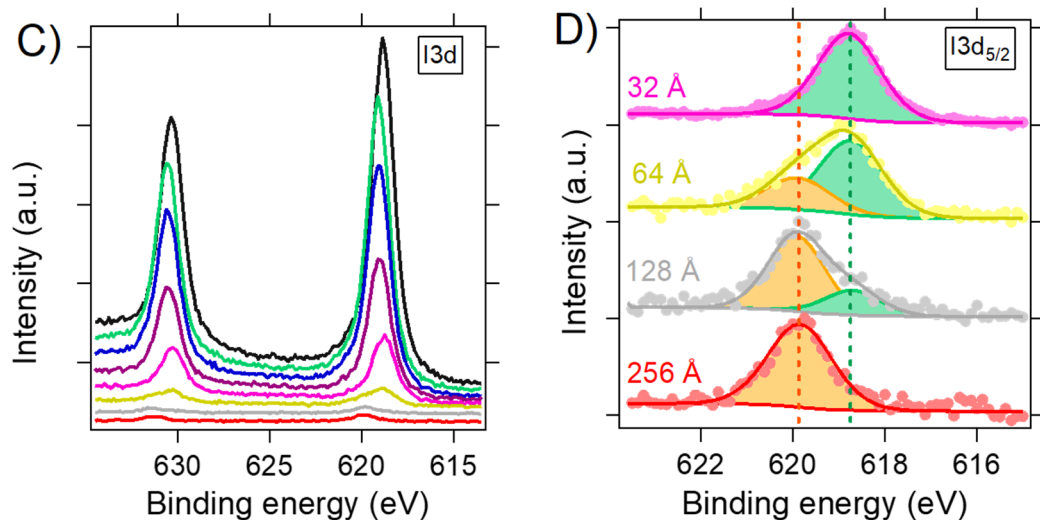


Figure 3. XPS data showing the C 1s (A), Sn 3d (B), and I 3d (C, D) regions during the stepwise deposition of C₆₀ on FASnI₃ with no surface ligand treatment.

The FASnI₃ energetics presented in the energy diagram are based on the UPS and IPES results, as the XPS results show a different trend. Here, the XPS results show a decrease of approximately 0.3 eV in the binding energy of all the FASnI₃ component peaks as the C₆₀ thickness is increased from 2 to 256 Å. These changes in XPS peak positions would suggest an upwards bending of the FASnI₃ VBM and CBM at the interface; however, the UPS and IPES results indicate a downwards bending of the VBM and relatively flat CBM. The IPES data does show a 0.1 eV increase in EA for FASnI₃ as the C₆₀ thickness increases to 16 Å, but accounting for the equivalent change in the WF results in a flat CBM. The result of these changes is a widening of the transport gap of FASnI₃ at the interface with C₆₀. Notably, the energetics of FASnI₃ near the interface should be favorable for reducing recombination due to the band bending occurring in the FASnI₃ VBM. We suspect that the depletion of I⁻ from the near-surface region of FASnI₃ and the resulting lattice distortions near the interface may be responsible for the

observed transport gap widening near the interface and the discrepancy with the XPS results, with the loss of I⁻ and lattice distortions disrupting the CB and VB more so than the core levels.

Next, surface ligands were employed to compare both the influence of the ligand binding group and the ligand tail on interfacial energetics and PV device performance and stability. These ligands include octanoic acid (OCA), a similar fluorinated derivative, 2*H*,2*H*,3*H*,3*H*-perfluorononanoic acid (FNCA), and trimethylphenylammonium chloride (TMPA-Cl). Both ammonium and carboxylic acid containing ligands have been applied to Pb-based HPs and they are expected to bind to the HP surface at different sites.^{39,64,65} Here, the ammonium groups can displace FA or fill FA vacancies at the surface, while the carboxylic acid groups can either displace I or fill I vacancies. The tail groups were selected to vary the energetics (e.g., FNCA vs. OCA), hydrophobicity, and electronic coupling between C₆₀ and FASnI₃.

The most common methods for surface ligand treatments are solution based,^{39,40,44,66} however, in this work we opted for a vapor treatment process which poses several advantages. The solution processability of FASnI₃ limits the solvents that can be used for surface treatment, and this need for orthogonal solvents severely limits the range of surface ligands that can be applied. Furthermore, solvent effects on the FASnI₃ films can lead to complications and may facilitate penetration of ligands into the bulk. A vapor treatment process following formation of FASnI₃ was chosen to circumvent these limitations and further details can be found in the experimental section.

XPS of the C1s region was used to probe surface ligand adsorption as displayed in **Figure 4**. The partially positively charged carbon in FA appears at approximately 288 eV and

shows good separation from adventitious carbon and the carbon species in many surface ligands that appear around 284.5 eV. Thus, the ratio of FA carbon to non-FA carbon is a good probe for the adsorption of surface ligands. In **Figure 4** fitting has been applied to identify the FA carbon (blue) and non-FA carbon (purple) species, with the values inside of the fitted regions indicating the relative peak areas. Note that satellite peaks from I 4d can be observed at the lower binding energy. These peaks are the result of cross contamination from Mg anode emission in the X-ray source. The un-treated FASnI₃ film displays a 1:1 ratio of FA to non-FA carbon, whereas the surface ligand treated FASnI₃ films show an increased amount of non-FA carbon. The FA to non-FA carbon for films treated with TMPA-Cl and OCA increases to 1:1.4 and 1:1.6. On the other hand, films treated with FNCA do not show a significant change in this ratio. This is because fluorination shifts the C peaks to higher BEs of *ca.* 291 eV (off scale, see SI **Figure S7A**) for CF₂ and CF₃ and about 286.83 eV for the spacer carbons between the carboxylic acid binding group and fluorinated tail. In this case F can be used as an additional probe for adsorption of FNCA, and as shown in SI **Figure S7B** a clear F1s peak is observed only in the FNCA modified film. No significant change in the Sn(II):Sn(IV) ratio is observed for any of the ligand treatments, with all FASnI₃ films showing a Sn(II):Sn(IV) ratio of approximately 12:1, as shown in SI **Figure S8**.

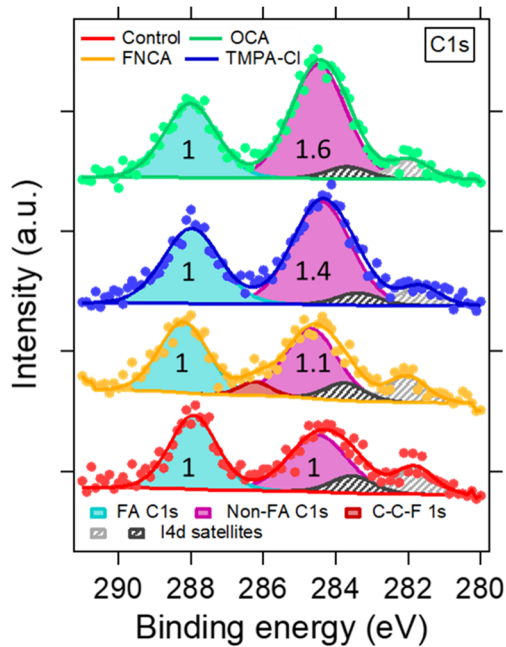


Figure 4. XPS showing the C region of FASnI₃ films following surface ligand treatment with FNCA, OCA, and TMPA-Cl. The numbers represent the integrated peak intensities, with the FA C peak normalized to 1.

To investigate the effects of surface ligands on the energetic structure at the Sn perovskite/C₆₀ interfaces, we performed the same series of incremental depositions of C₆₀ accompanied by UPS, XPS, and IPES measurements at each thickness increment on FASnI₃ samples treated with FNCA, OCA, and TMPA-Cl. Two of the modifiers, OCA and TMPA-Cl, showed similar results as the un-treated film, and thus we focus the bulk of this discussion on the FNCA treated FASnI₃ interface. **Figure 5A** and **B** show the evolution of the UPS and IPES spectra on a semilogarithmic plot for the FNCA modified film as the thickness of C₆₀ is increased from 0 to 256 Å. The FNCA treated film shows a 0.18 eV increase in the work function from 4.83 to 5.01 eV, which is most likely due to the surface dipole introduced by FNCA. The work function shift between the untreated and FNCA treated FASnI₃ is less than

may be expected if a monolayer of a heavily fluorinated alkane was present on the surface,⁶⁷ which is attributed to the formation of only a partial monolayer. As detailed in the Supporting Information, the surface coverage of FNCA is estimated at 20 to 40% based on angle dependent XPS data (SI **Figure S9**). Using the same fitting methods as described for the neat FASnI₃ film, the IE and EA for the FNCA modified film are found to be 5.51 eV and 4.03 eV, respectively. This corresponds with a 0.2 eV increase in IE and a 0.1 eV increase in EA after treatment with FNCA. The difference between the IE and EA values give a transport gap of 1.48 eV, which deviates more from the optical gap and is slightly larger than the transport gap of neat FASnI₃. The energy diagram in **Figure 5C** was constructed from a combination of the UPS, IPES, and XPS data and shows the evolution of the FASnI₃-FNCA and C₆₀ energetics from 0-16 Å and 8-256 Å respectively.

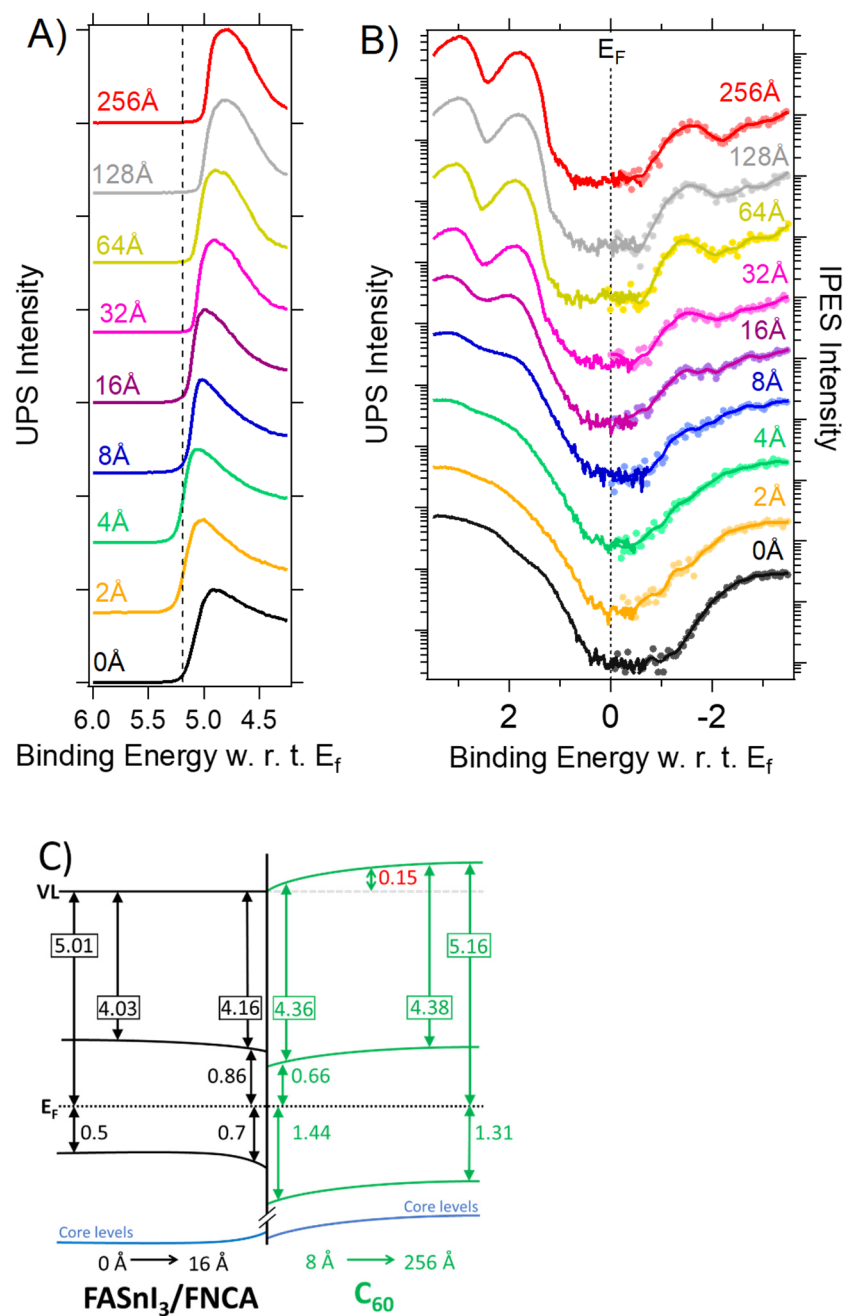


Figure 5. Secondary electron cutoff region (A) and onset region (B) recorded using UPS and IPES during the stepwise deposition of C_{60} on $FASnI_3$ with FNCA surface ligand treatment. Results are summarized in a schematic diagram of the energy levels (C). Work functions were determined from the SECO in UPS.

The XPS spectra taken at each thickness increment during the deposition of C₆₀ on FNCA-FASnI₃ are displayed in **Figure 6**. Here, all XPS peaks from FASnI₃ shift by approximately 0.3 eV towards lower binding energies as the C₆₀ thickness is increased from 0 to 32 Å, which is similar to the shifts observed for unmodified FASnI₃ as the C₆₀ thickness is increased from 2 to 32 Å. However, the FNCA-treated FASnI₃ does not show the initial increase in BE of 0.2 to 0.3 eV upon deposition of 2 Å C₆₀ that was observed for the un-treated film. Attenuation of the Sn and I peaks follow the same trend as observed in the non-modified FASnI₃ film, where Sn is absent in the XPS spectra after 128 Å of C₆₀ has been deposited, but I remains visible through 256 Å. Likewise the position of the I peaks at the final thickness are approximately 1 eV higher and the same evolution of the I 3d_{5/2} peak as presented in **Figure 3D** is observed. Further, comparison of the C:I ratio at C₆₀ thicknesses of 64 Å and greater shows essentially no change from the control at 330:1. These results indicate that FNCA treatment has little effect on the diffusion of I⁻ into the C₆₀ layer. The inability of FNCA to reduce or prevent I⁻ diffusion is attributed to the incomplete surface coverage of FNCA.

The energy diagram shows that despite the changes in the FASnI₃ CBM and VBM after FNCA treatment, the LUMO and HOMO of C₆₀ remain offset in favorable positions for electron transfer from FASnI₃ to C₆₀. Similar to un-treated FASnI₃, both the HOMO and LUMO bands of C₆₀ display upward band bending as the thickness increases. Again, the UPS results are at odds with the XPS results with regards to the FASnI₃ VBM shift at the interface. Here, UPS results show that the VBM moves away from E_F as the C₆₀ thickness is increased, but XPS results show that the core level energies move closer towards E_F as the C₆₀ thickness is increased.

Stepwise C₆₀ depositions with UPS, IPES, and XPS measurements were recorded for TMPA-Cl and OCA treated FASnI₃ as well. These results, as displayed in SI **Figures S10 and S11**, show that little change is observed upon treatment with surface ligands, that is the work function, IE, and EA values vary by less than 0.1 eV from the neat FASnI₃ film. As additional C₆₀ is deposited similar trends are observed as seen with untreated FASnI₃ and both show evidence of I⁻ diffusion into C₆₀ as shown in SI **Figure S12**. In general, all the examined interfaces show a favorable energy landscape for electron transfer from FASnI₃ to C₆₀, widening of the FASnI₃ transport gap at the interface with C₆₀, small increases in the work function upon increasing C₆₀ thickness, and band bending in both C₆₀ and FASnI₃.

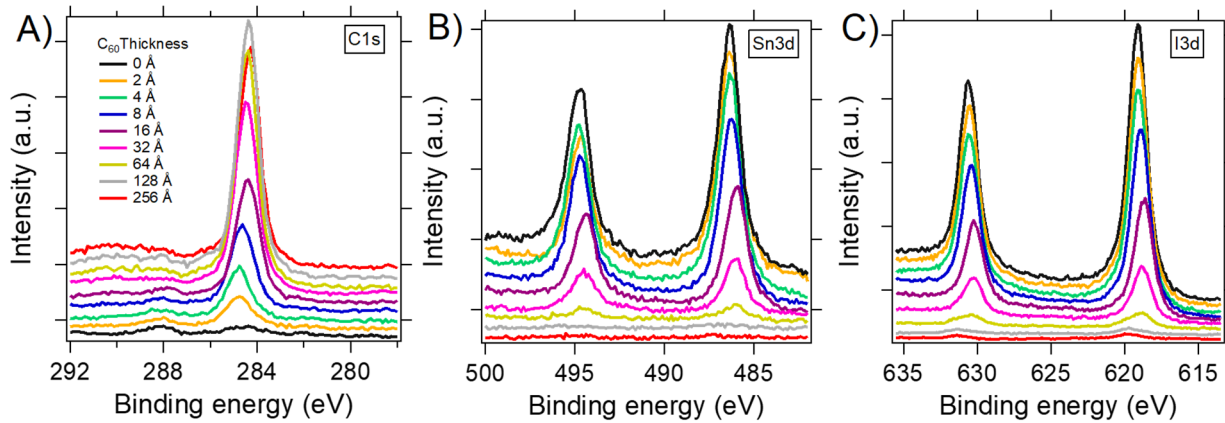


Figure 6. XPS data showing the C 1s (A), Sn 3d (B), and I 3d (C) regions during the stepwise deposition of C₆₀ on FASnI₃ with FNCA ligand exposure

To examine how altering the interfacial energetics through treatment with surface ligands affects interfacial charge transfer processes, photovoltaic devices were fabricated with the architecture ITO/PEDOT:PSS/FASnI₃+surface ligand/C₆₀/BCP/Ag, both with and without surface ligand treatment of the FASnI₃. The max (average) efficiency achieved with non-

modified FASnI₃ was 4.98 (4.71)%, 3.76 (3.5)% for OCA, 4.38 (3.83)% for FNCA, and 5.93 (5.55)% for TMPA-Cl. Some of these best PV devices were achieved in different fabrication sets completed over a period of four months and significant set-to-set variations were observed, which is related to the sensitive nature of FASnI₃ fabrication and ligand treatment. Based on multiple comparisons within single sets of devices, the surface ligands TMPA-Cl and FNCA typically increase PCE, whereas OCA typically results in similar PCE as the non-modified device. A common trend observed with the highest performing devices containing TMPA-Cl and FNCA surface ligands is an improvement in the open circuit voltage (V_{oc}), with the best PV devices showing V_{oc} increases of 0.1 and 0.08 V, respectively, compared to un-treated devices. In the direct side-by-side comparison shown in **Figure 7**, only FNCA displays a statistically significant increase in V_{oc} , whereas both FNCA and OCA show marginal improvements in short circuit current density (J_{sc}).

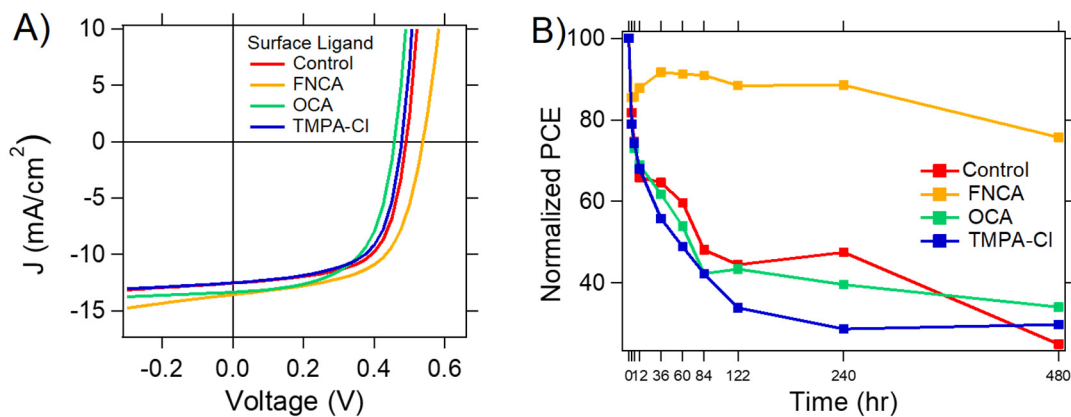


Figure 7. Current-voltage curves measured under AM1.5 simulated irradiation for the PV devices with various surface ligand treatments (A) and the PCE of the PV devices as function of time after device fabrication (B).

The PV device results may in part be rationalized through the changes observed in the interfacial energetics. All FASnI₃/C₆₀ interfaces, with and without surface ligands, retain favorable energy level offsets for electron transfer from FASnI₃ to C₆₀, thus no appreciable loss in PV device performance is expected. However, the improvements observed for devices that contain TMPA-Cl and FNCA may be ascribed to subtle changes in the interfacial energetics. For instance, at TMPA-Cl and FNCA modified interfaces the FASnI₃ conduction band shows more pronounced downward bending of 0.11 and 0.12 eV, respectively, which may promote photogenerated electron migration from the FASnI₃ bulk to the interface with C₆₀. This bending in the FASnI₃ conduction band is not observed for the untreated or OCA treated interfaces. Further, the overall vacuum level shifts observed upon C₆₀ deposition with TMPA-Cl and FNCA modified films is reduced compared to the untreated and OCA treated films. The LUMO bending in C₆₀ and the vacuum level shifts should result in increased electron accumulation at the interface with FASnI₃; thereby, the more minimal shifts in the FNCA and TMPA-Cl treated films are suspected to benefit PV performance by reducing the electron density at the FASnI₃ interface.

To investigate the impact of surface ligands on device stability a single device set was fabricated using all surface ligands and the devices were tested as a function of time after device completion to monitor the degradation of device performance. **Figure 7** shows JV curves for the best PV devices with each surface ligand obtained in this set and the normalized change in average PCE as a function of time. During this measurement series, the devices were stored and tested in a nitrogen filled glovebox with O₂ and H₂O levels below 0.2 and 0.5 ppm, respectively. Over the first three hours all device averages drop sharply, after which a slower decay

component begins. Non-modified devices degrade rapidly: reaching 50% of their original PCE by approximately the 60-hour mark. Devices treated with OCA and TMPA-Cl show similar instability; however, those treated with FNCA show significantly improved stability. After 10 and 20 days of storage the average PCE remains above 90 and 75% of the initial value, respectively. We suspect that the increased stability upon FNCA treatment is due to the hydrophobic nature of the heavily fluorinated tail group, which can help reduce degradation reactions with water. These results highlight the promise of using surface ligands to stabilize the PV performance of Sn-based HPs.

Conclusions:

The FASnI₃/C₆₀ interfaces, both with and without surface ligands, all display favorable energy landscapes for electron transfer from FASnI₃ to C₆₀. The widening of the FASnI₃ transport gap at the C₆₀ interface and the disagreement in the core level and valence band shifts relative to E_F highlights that significant changes are occurring in the electronic structure of FASnI₃ at this interface, which may have a significant influence on PV performance. In part, these electronic structure changes may be attributed to I⁻ diffusion out of FASnI₃ and into C₆₀. Currently, the influence of I⁻ diffusion and *n*-doping of C₆₀ on interfacial energetics, charge transfer, and PV performance are unclear and are a subject of active investigation in our group. The observation that the surface ligand FNCA can greatly improve the stability of FASnI₃-based PSCs, even though it does not inhibit I⁻ diffusion, emphasizes the potential importance of surface ligands and underscores the need to better determine degradation mechanisms in Sn-based PSCs.

ASSOCIATED CONTENT

Supporting Information. Supporting information includes ultraviolet, inverse, and X-ray photoelectron spectra, UV-Vis absorbance and photoluminescence spectra, examples of the fitting routine applied to the photoelectron spectra, angle dependent XPS data, calculations of iodide diffusion, and UPS and IPES data recorded during the step-wise deposition of C₆₀ on FASnI₃.

AUTHOR INFORMATION

Corresponding Author

*E-mail: kenneth.graham@uky.edu

Author Contributions

The manuscript was written through contributions of all authors. All authors have given approval to the final version of the manuscript.

Funding Sources

This material is based upon work supported by the U.S. Department of Energy, Office of Science, Office of Basic Energy Sciences, and the EPSCoR program, under award no.

DE-SC0018208.

ACKNOWLEDGMENT

We gratefully acknowledge the U.S. Department of Energy, Office of Science, Office of Basic Energy Sciences, and the EPSCoR program, under award no. DE-SC0018208.

REFERENCES

- (1) Schulz, P.; Cahen, D.; Kahn, A. Halide Perovskites: Is It All about the Interfaces? *Chem. Rev.* **2019**, *119*, 3349–3417.
- (2) Yang, Y.; Yang, M.; Moore, D. T.; Yan, Y.; Miller, E. M.; Zhu, K.; Beard, M. C. Top and Bottom Surfaces Limit Carrier Lifetime in Lead Iodide Perovskite Films. *Nat. Energy* **2017**, *2*, 16207.
- (3) Yang, Y.; Yan, Y.; Yang, M.; Choi, S.; Zhu, K.; Luther, J. M.; Beard, M. C. Low Surface Recombination Velocity in Solution-Grown CH₃NH₃PbBr₃ Perovskite Single Crystal. *Nat. Commun.* **2015**, *6*, 7961.
- (4) Murali, B.; Yengel, E.; Yang, C.; Peng, W.; Alarousu, E.; Bakr, O. M.; Mohammed, O. F. The Surface of Hybrid Perovskite Crystals: A Boon or Bane. *ACS Energy Lett.* **2017**, *2*, 846–856.
- (5) Sherkar, T. S.; Momblona, C.; Gil-Escrig, L.; Bolink, H. J.; Koster, L. J. A. Improving Perovskite Solar Cells: Insights From a Validated Device Model. *Adv. Energy Mater.* **2017**, *7*, 1602432.
- (6) Sherkar, T. S.; Momblona, C.; Gil-Escrig, L.; Ávila, J.; Sessolo, M.; Bolink, H. J.; Koster, L. J. A. Recombination in Perovskite Solar Cells: Significance of Grain Boundaries, Interface Traps, and Defect Ions. *ACS Energy Lett.* **2017**, *2*, 1214–1222.
- (7) Zohar, A.; Kulbak, M.; Levine, I.; Hodes, G.; Kahn, A.; Cahen, D. What Limits the Open-Circuit Voltage of Bromide Perovskite-Based Solar Cells? *ACS Energy Lett.* **2019**, *4*, 1–7.
- (8) Wang, J.; Fu, W.; Jariwala, S.; Sinha, I.; Jen, A. K.-Y.; Ginger, D. S. Reducing Surface Recombination Velocities at the Electrical Contacts Will Improve Perovskite Photovoltaics. *ACS Energy Lett.* **2019**, *4*, 222–227.
- (9) Sarritsu, V.; Sestu, N.; Marongiu, D.; Chang, X.; Masi, S.; Rizzo, A.; Colella, S.; Quochi, F.; Saba, M.; Mura, A.; Bongiovanni, G. Optical Determination of Shockley-Read-Hall and Interface Recombination Currents in Hybrid Perovskites. *Sci. Rep.* **2017**, *7*, 44629.

- (10) Stolterfoht, M.; Caprioglio, P.; Wolff, C. M.; Márquez, J. A.; Nordmann, J.; Zhang, S.; Rothhardt, D.; Hörmann, U.; Amir, Y.; Redinger, A.; Kegelmann, L.; Zu, F.; Albrecht, S.; Koch, N.; Kirchartz, T.; Saliba, M.; Unold, T.; Neher, D. The Impact of Energy Alignment and Interfacial Recombination on the Internal and External Open-Circuit Voltage of Perovskite Solar Cells. *Energy Environ. Sci.* **2019**, *12*, 2778–2788.
- (11) Zhao, L.; Kerner, R. A.; Xiao, Z.; Lin, Y. L.; Lee, K. M.; Schwartz, J.; Rand, B. P. Redox Chemistry Dominates the Degradation and Decomposition of Metal Halide Perovskite Optoelectronic Devices. *ACS Energy Lett.* **2016**, *1*, 595–602.
- (12) Kojima, A.; Teshima, K.; Shirai, Y.; Miyasaka, T. Organometal Halide Perovskites as Visible-Light Sensitizers for Photovoltaic Cells. *J. Am. Chem. Soc.* **2009**, *131*, 6050–6051.
- (13) Jena, A. K.; Kulkarni, A.; Miyasaka, T. Halide Perovskite Photovoltaics: Background, Status, and Future Prospects. *Chem. Rev.* **2019**, *119*, 3036–3103.
- (14) DeQuilettes, D. W.; Koch, S.; Burke, S.; Paranjli, R. K.; Shropshire, A. J.; Ziffer, M. E.; Ginger, D. S. Photoluminescence Lifetimes Exceeding 8 μ s and Quantum Yields Exceeding 30% in Hybrid Perovskite Thin Films by Ligand Passivation. *ACS Energy Lett.* **2016**, *1*, 438–444.
- (15) Yang, J.-M.; Luo, Y.; Bao, Q.; Li, Y.-Q.; Tang, J.-X. Recent Advances in Energetics and Stability of Metal Halide Perovskites for Optoelectronic Applications. *Adv. Mater. Interfaces* **2019**, *6*, 1801351.
- (16) Olthof, S. Research Update: The Electronic Structure of Hybrid Perovskite Layers and Their Energetic Alignment in Devices. *APL Mater.* **2016**, *4*, 091502.
- (17) Jeong, J.; Kang, D.; Chun, D. H.; Shin, D.; Park, J. H.; Cho, S. W.; Jeong, K.; Lee, H.; Yi, Y. Unveiling the Origin of Performance Reduction in Perovskite Solar Cells with TiO₂ Electron Transport Layer: Conduction Band Minimum Mismatches and Chemical Interactions at Buried Interface. *Appl. Surf. Sci.* **2019**, *495*, 143490.

- (18) Correa Baena, J. P.; Steier, L.; Tress, W.; Saliba, M.; Neutzner, S.; Matsui, T.; Giordano, F.; Jacobsson, T. J.; Srimath Kandada, A. R.; Zakeeruddin, S. M.; Petrozza, A.; Abate, A.; Nazeeruddin, M. K.; Grätzel, M.; Hagfeldt, A. Highly Efficient Planar Perovskite Solar Cells through Band Alignment Engineering. *Energy Environ. Sci.* **2015**, *8*, 2928–2934.
- (19) Schulz, P.; Whittaker-Brooks, L. L.; MacLeod, B. A.; Olson, D. C.; Loo, Y.-L.; Kahn, A. Electronic Level Alignment in Inverted Organometal Perovskite Solar Cells. *Adv. Mater. Interfaces* **2015**, *2*, 1400532.
- (20) Liu, X.; Wang, C.; Lyu, L.; Wang, C.; Xiao, Z.; Bi, C.; Huang, J.; Gao, Y. Electronic Structures at the Interface between Au and CH₃NH₃PbI₃. *Phys. Chem. Chem. Phys.* **2015**, *17*, 896–902.
- (21) Chen, S.; Goh, T. W.; Sabba, D.; Chua, J.; Mathews, N.; Huan, C. H. A.; Sum, T. C. Energy Level Alignment at the Methylammonium Lead Iodide/Copper Phthalocyanine Interface. *APL Mater.* **2014**, *2*, 081512.
- (22) Endres, J.; Kulbak, M.; Zhao, L.; Rand, B. P.; Cahen, D.; Hodes, G.; Kahn, A. Electronic Structure of the CsPbBr₃/Polytriarylamine (PTAA) System. *J. Appl. Phys.* **2017**, *121*, 035304.
- (23) Schulz, P.; Edri, E.; Kirmayer, S.; Hodes, G.; Cahen, D.; Kahn, A. Interface Energetics in Organo-Metal Halide Perovskite-Based Photovoltaic Cells. *Energy Environ. Sci.* **2014**, *7*, 1377.
- (24) Ji, G.; Zheng, G.; Zhao, B.; Song, F.; Zhang, X.; Shen, K.; Yang, Y.; Xiong, Y.; Gao, X.; Cao, L.; Qi, D.-C. Interfacial Electronic Structures Revealed at the Rubrene/CH₃NH₃PbI₃ Interface. *Phys. Chem. Chem. Phys.* **2017**, *19*, 6546–6553.
- (25) Hawash, Z.; Raga, S. R.; Son, D.-Y.; Ono, L. K.; Park, N.-G.; Qi, Y. Interfacial Modification of Perovskite Solar Cells Using an Ultrathin MAI Layer Leads to Enhanced Energy Level Alignment, Efficiencies, and Reproducibility. *J. Phys. Chem. Lett.* **2017**, *8*, 3947–3953.

- (26) Wang, Q.-K.; Wang, R.-B.; Shen, P.-F.; Li, C.; Li, Y.-Q.; Liu, L.-J.; Duhm, S.; Tang, J.-X. Energy Level Offsets at Lead Halide Perovskite/Organic Hybrid Interfaces and Their Impacts on Charge Separation. *Adv. Mater. Interfaces* **2015**, *2*, 1400528.
- (27) Endres, J.; Kulbak, M.; Zhao, L.; Rand, B. P.; Cahen, D.; Hodes, G.; Kahn, A. Electronic Structure of the CsPbBr₃/Polytriarylamine (PTAA) System. *J. Appl. Phys.* **2017**, *121*, 35304.
- (28) Lo, M.-F.; Guan, Z.-Q.; Ng, T.-W.; Chan, C.-Y.; Lee, C.-S. Electronic Structures and Photoconversion Mechanism in Perovskite/Fullerene Heterojunctions. *Adv. Funct. Mater.* **2015**, *25*, 1213–1218.
- (29) Wang, C.; Wang, C.; Liu, X.; Kauppi, J.; Shao, Y.; Xiao, Z.; Bi, C.; Huang, J.; Gao, Y. Electronic Structure Evolution of Fullerene on CH₃NH₃PbI₃. *Appl. Phys. Lett.* **2015**, *106*.
- (30) Zu, F.; Amsalem, P.; Ralaiarisoa, M.; Schultz, T.; Schlesinger, R.; Koch, N. Surface State Density Determines the Energy Level Alignment at Hybrid Perovskite/Electron Acceptors Interfaces. *ACS Appl. Mater. Interfaces* **2017**, *9*, 41546–41552.
- (31) Miller, E. M.; Zhao, Y.; Mercado, C. C.; Saha, S. K.; Luther, J. M.; Zhu, K.; Stevanović, V.; Perkins, C. L.; van de Lagemaat, J. Substrate-Controlled Band Positions in CH₃NH₃PbI₃ Perovskite Films. *Phys. Chem. Chem. Phys.* **2014**, *16*, 22122–22130.
- (32) Tao, S.; Schmidt, I.; Brocks, G.; Jiang, J.; Tranca, I.; Meerholz, K.; Olthof, S. Absolute Energy Level Positions in Tin- and Lead-Based Halide Perovskites. *Nat. Commun.* **2019**, *10*, 2560.
- (33) Endres, J.; Egger, D. A.; Kulbak, M.; Kerner, R. A.; Zhao, L.; Silver, S. H.; Hodes, G.; Rand, B. P.; Cahen, D.; Kronik, L.; Kahn, A. Valence and Conduction Band Densities of States of Metal Halide Perovskites: A Combined Experimental–Theoretical Study. *J. Phys. Chem. Lett.* **2016**, *7*, 2722–2729.
- (34) Zu, F.; Wolff, C. M.; Ralaiarisoa, M.; Amsalem, P.; Neher, D.; Koch, N. Unraveling the

- Electronic Properties of Lead Halide Perovskites with Surface Photovoltage in Photoemission Studies. *ACS Appl. Mater. Interfaces* **2019**, *11*, 21578–21583.
- (35) Zhang, F.; Ullrich, F.; Silver, S.; Kerner, R. A.; Rand, B. P.; Kahn, A. Complexities of Contact Potential Difference Measurements on Metal Halide Perovskite Surfaces. *J. Phys. Chem. Lett.* **2019**, *10*, 890–896.
- (36) Zu, F.-S.; Amsalem, P.; Salzmann, I.; Wang, R.-B.; Ralaiarisoa, M.; Kowarik, S.; Duhm, S.; Koch, N. Impact of White Light Illumination on the Electronic and Chemical Structures of Mixed Halide and Single Crystal Perovskites. *Adv. Opt. Mater.* **2017**, *5*, 1700139.
- (37) Wolff, C. M.; Zu, F.; Paulke, A.; Toro, L. P.; Koch, N.; Neher, D. Reduced Interface-Mediated Recombination for High Open-Circuit Voltages in CH₃NH₃PbI₃ Solar Cells. *Adv. Mater.* **2017**, *29*, 1700159.
- (38) Shin, D.; Kang, D.; Jeong, J.; Park, S.; Kim, M.; Lee, H.; Yi, Y. Unraveling the Charge Extraction Mechanism of Perovskite Solar Cells Fabricated with Two-Step Spin Coating: Interfacial Energetics between Methylammonium Lead Iodide and C₆₀. *J. Phys. Chem. Lett.* **2017**, *8*, 5423–5429.
- (39) Wang, F.; Geng, W.; Zhou, Y.; Fang, H.-H.; Tong, C.-J.; Loi, M. A.; Liu, L.-M.; Zhao, N. Phenylalkylamine Passivation of Organolead Halide Perovskites Enabling High-Efficiency and Air-Stable Photovoltaic Cells. *Adv. Mater.* **2016**, *28*, 9986–9992.
- (40) Noel, N. K.; Abate, A.; Stranks, S. D.; Parrott, E. S.; Burlakov, V. M.; Goriely, A.; Snaith, H. J. Enhanced Photoluminescence and Solar Cell Performance via Lewis Base Passivation of Organic–Inorganic Lead Halide Perovskites. *ACS Nano* **2014**, *8*, 9815–9821.
- (41) Koscher, B. A.; Swabeck, J. K.; Bronstein, N. D.; Alivisatos, A. P. Essentially Trap-Free CsPbBr₃ Colloidal Nanocrystals by Postsynthetic Thiocyanate Surface Treatment. *J. Am. Chem. Soc.* **2017**, *139*, 6566–6569.
- (42) Uddin, M. A.; Mobley, J. K.; Masud, A. A.; Liu, T.; Calabro, R. L.; Kim, D.-Y.; Richards,

- C. I.; Graham, K. R. Mechanistic Exploration of Dodecanethiol-Treated Colloidal CsPbBr₃ Nanocrystals with Photoluminescence Quantum Yields Reaching Near 100%. *J. Phys. Chem. C* **2019**, *123*, 18103–18112.
- (43) Zuo, L.; Chen, Q.; De Marco, N.; Hsieh, Y.-T.; Chen, H.; Sun, P.; Chang, S.-Y.; Zhao, H.; Dong, S.; Yang, Y. Tailoring the Interfacial Chemical Interaction for High-Efficiency Perovskite Solar Cells. *Nano Lett.* **2017**, *17*, 269–275.
- (44) Wang, S.; Zhu, Y.; Wang, C.; Ma, R. Interface Modification by a Multifunctional Ammonium Salt for High Performance and Stable Planar Perovskite Solar Cells. *J. Mater. Chem. A* **2019**, *7*, 11867–11876.
- (45) Ke, W.; Stoumpos, C. C.; Spanopoulos, I.; Chen, M.; Wasielewski, M. R.; Kanatzidis, M. G. Diammonium Cations in the FASnI₃ Perovskite Structure Lead to Lower Dark Currents and More Efficient Solar Cells. *ACS Energy Lett.* **2018**, *3*, 1470–1476.
- (46) Shao, S.; Liu, J.; Portale, G.; Fang, H.-H.; Blake, G. R.; ten Brink, G. H.; Koster, L. J. A.; Loi, M. A. Highly Reproducible Sn-Based Hybrid Perovskite Solar Cells with 9% Efficiency. *Adv. Energy Mater.* **2018**, *8*, 1702019.
- (47) Boehm, A. M.; Wieser, J.; Butrouna, K.; Graham, K. R. A New Photon Source for Ultraviolet Photoelectron Spectroscopy of Organic and Other Damage-Prone Materials. *Org. Electron.* **2017**, *41*, 9–16.
- (48) Leijtens, T.; Prasanna, R.; Gold-Parker, A.; Toney, M. F.; McGehee, M. D. Mechanism of Tin Oxidation and Stabilization by Lead Substitution in Tin Halide Perovskites. *ACS Energy Lett.* **2017**, *2*, 2159–2165.
- (49) Yoshida, H. Near-Ultraviolet Inverse Photoemission Spectroscopy Using Ultra-Low Energy Electrons. *Chem. Phys. Lett.* **2012**, *539–540*, 180–185.
- (50) Ke, W.; Stoumpos, C. C.; Logsdon, J. L.; Wasielewski, M. R.; Yan, Y.; Fang, G.; Kanatzidis, M. G. TiO₂-ZnS Cascade Electron Transport Layer for Efficient

- Formamidinium Tin Iodide Perovskite Solar Cells. *J. Am. Chem. Soc.* **2016**, *138*, 14998–15003.
- (51) Liu, J.; Ozaki, M.; Yakumar, S.; Handa, T.; Nishikubo, R.; Kanemitsu, Y.; Saeki, A.; Murata, Y.; Murdey, R.; Wakamiya, A. Lead-Free Solar Cells Based on Tin Halide Perovskite Films with High Coverage and Improved Aggregation. *Angew. Chemie Int. Ed.* **2018**, *57*, 13221–13225.
- (52) Koh, T. M.; Krishnamoorthy, T.; Yantara, N.; Shi, C.; Leong, W. L.; Boix, P. P.; Grimsdale, A. C.; Mhaisalkar, S. G.; Mathews, N. Formamidinium Tin-Based Perovskite with Low E_g for Photovoltaic Applications. *J. Mater. Chem. A* **2015**, *3*, 14996–15000.
- (53) Xi, J.; Wu, Z.; Jiao, B.; Dong, H.; Ran, C.; Piao, C.; Lei, T.; Song, T.-B.; Ke, W.; Yokoyama, T.; Hou, X.; Kanatzidis, M. G. Multichannel Interdiffusion Driven FASnI_3 Film Formation Using Aqueous Hybrid Salt/Polymer Solutions toward Flexible Lead-Free Perovskite Solar Cells. *Adv. Mater.* **2017**, *29*, 1606964.
- (54) Wang, R.; Wu, C.; Hu, Y.; Li, J.; Shen, P.; Wang, Q.; Liao, L.; Liu, L.; Duhm, S. $\text{CH}_3\text{NH}_3\text{PbI}_{3-x}\text{Cl}_x$ under Different Fabrication Strategies: Electronic Structures and Energy-Level Alignment with an Organic Hole Transport Material. *ACS Appl. Mater. Interfaces* **2017**, *9*, 7859–7865.
- (55) Park, S. M.; Mazza, S. M.; Liang, Z.; Abtahi, A.; Boehm, A. M.; Parkin, S. R.; Anthony, J. E.; Graham, K. R. Processing Dependent Influence of the Hole Transport Layer Ionization Energy on Methylammonium Lead Iodide Perovskite Photovoltaics. *ACS Appl. Mater. Interfaces* **2018**, *10*, 15548–15557.
- (56) Wang, C.; Wang, C.; Liu, X.; Kauppi, J.; Shao, Y.; Xiao, Z.; Bi, C.; Huang, J.; Gao, Y. Electronic Structure Evolution of Fullerene on $\text{CH}_3\text{NH}_3\text{PbI}_3$. *Appl. Phys. Lett.* **2015**, *106*, 111603.
- (57) Chang, C.-Y.; Huang, W.-K.; Chang, Y.-C.; Lee, K.-T.; Chen, C.-T. A Solution-Processed n-Doped Fullerene Cathode Interfacial Layer for Efficient and Stable Large-Area

- Perovskite Solar Cells. *J. Mater. Chem. A* **2016**, *4*, 640–648.
- (58) Li, C.-Z.; Chueh, C.-C.; Ding, F.; Yip, H.-L.; Liang, P.-W.; Li, X.; Jen, A. K.-Y. Doping of Fullerenes via Anion-Induced Electron Transfer and Its Implication for Surfactant Facilitated High Performance Polymer Solar Cells. *Adv. Mater.* **2013**, *25*, 4425–4430.
- (59) Bai, Y.; Dong, Q.; Shao, Y.; Deng, Y.; Wang, Q.; Shen, L.; Wang, D.; Wei, W.; Huang, J. Enhancing Stability and Efficiency of Perovskite Solar Cells with Crosslinkable Silane-Functionalized and Doped Fullerene. *Nat. Commun.* **2016**, *7*, 12806.
- (60) Sun, X.; Ji, L. Y.; Chen, W. W.; Guo, X.; Wang, H. H.; Lei, M.; Wang, Q.; Li, Y. F. Halide Anion–Fullerene π Noncovalent Interactions: N-Doping and a Halide Anion Migration Mechanism in p–i–n Perovskite Solar Cells. *J. Mater. Chem. A* **2017**, *5*, 20720–20728.
- (61) Jiao, W.; Ma, D.; Lv, M.; Chen, W.; Wang, H.; Zhu, J.; Lei, M.; Chen, X. Self N-Doped [6,6]-Phenyl-C61-Butyric Acid 2-((2-(Trimethylammonium)Ethyl)-(Dimethyl)Ammonium) Ethyl Ester Diiodides as a Cathode Interlayer for Inverted Polymer Solar Cells. *J. Mater. Chem. A* **2014**, *2*, 14720–14728.
- (62) Chen, W.; Jiao, W.; Li, D.; Sun, X.; Guo, X.; Lei, M.; Wang, Q.; Li, Y. Cross Self-n-Doping and Electron Transfer Model in a Stable and Highly Conductive Fullerene Ammonium Iodide: A Promising Cathode Interlayer in Organic Solar Cells. *Chem. Mater.* **2016**, *28*, 1227–1235.
- (63) Lo, M.-F.; Guan, Z.-Q.; Ng, T.-W.; Chan, C.-Y.; Lee, C.-S. Electronic Structures and Photoconversion Mechanism in Perovskite/Fullerene Heterojunctions. *Adv. Funct. Mater.* **2015**, *25*, 1213–1218.
- (64) Yang, S.; Wang, Y.; Liu, P.; Cheng, Y.-B.; Zhao, H. J.; Yang, H. G. Functionalization of Perovskite Thin Films with Moisture-Tolerant Molecules. *Nat. Energy* **2016**, *1*, 15016.
- (65) Grancini, G.; Roldán-Carmona, C.; Zimmermann, I.; Mosconi, E.; Lee, X.; Martineau, D.; Nabey, S.; Oswald, F.; De Angelis, F.; Graetzel, M.; Nazeeruddin, M. K. One-Year Stable

Perovskite Solar Cells by 2D/3D Interface Engineering. *Nat. Commun.* **2017**, *8*, 15684.

- (66) Du, X.; Qiu, R.; Zou, T.; Chen, X.; Chen, H.; Zhou, H. Enhanced Uniformity and Stability of Pb–Sn Perovskite Solar Cells via Me₄NBr Passivation. *Adv. Mater. Interfaces* **2019**, *6*, 1900413.
- (67) Alloway, D. M.; Hofmann, M.; Smith, D. L.; Gruhn, N. E.; Graham, A. L.; Colorado, R.; Wysocki, V. H.; Lee, T. R.; Lee, P. A.; Armstrong, N. R. Interface Dipoles Arising from Self-Assembled Monolayers on Gold: UV-Photoemission Studies of Alkanethiols and Partially Fluorinated Alkanethiols. *J. Phys. Chem. B* **2003**, *107*, 11690–11699.

TOC Figure

